PHYSICAL SCIENCES

Ant waves—Spontaneous activity waves in fire-ant columns

Caleb Anderson[1,2], Guillermo Goldsztein[3], Alberto Fernandez-Nieves[1,2,4,5]*

Active matter, which includes crowds of organisms, is composed of constituents that independently consume and dissipate energy. Some active matter systems have been shown to sustain the propagation of various types of waves, resulting from the interplay between density and alignment. Here, we examine a type of solitary wave in dense two-dimensional columns of *Solenopsis invicta*, fire ants, in which the local activity, density and alignment all play a key role. We demonstrate that these waves are nonlinear and that they are composed of aligned ants that are constrained at the top by the time it takes disordered ants to activate and align and at the bottom by a density minimum enforced by gravity. Our results suggest that intrinsically switchable activity can be a productive framework to understand and trigger a broad range of wave-like behaviors, including stampedes in crowds and herds.

INTRODUCTION

Flocks of birds (*1*, *2*), swarming colonies of bacteria (*3*, *4*), and collectives of fire ants (*5–7*) are all composed of individuals that take advantage of their internal metabolism to self-propel. The constant energy input and dissipation at the single-particle level drive active matter systems such as these far from equilibrium so that the usual rules of thermodynamics need not apply (*8*, *9*). Much of our understanding of their behavior has come from studying simple model active systems, which are usually controlled by two parameters: density and orientational noise. For example, Vicsek-type simulations show that decreasing orientational noise or increasing the density in a system of constant-speed self-propelled particles with local alignment interactions results in a dynamic phase transition to a collective motion or flocking phase (*10*, *11*). At low density or high noise, self-propelled particles move with statistically random orientations, but as the density of the particles increases or the noise decreases, the symmetry of the system is spontaneously broken, and the particles align to create a phase with nonzero average velocity. In everyday experience, we see this in dense flocks of birds or schools of fish (*12*) that align and travel as a group. Further work has shown that systems of self-propelled particles can support several types of density waves, including sound waves (*13–15*), rationalized as linear perturbations of the Toner-Tu continuum equations, which are the analog of the Navier-Stokes equations for active fluids, and traveling polar bands (*16–19*), which we associate with a dense phase of aligned particles that propagate through another disordered and dilute background phase (*20*, *21*). Here, we introduce an unexpected type of mixed activity/density/alignment nonlinear wave in two-dimensional (2D) columns of *Solenopsis invicta* or fire ants.

RESULTS

High-density collectives of fire ants are common immediately after floods, which the ants survive by forming living rafts that are often just one or two ants thick. Inspired by both work on fire-ant rafts (*22–24*) and work on sedimentation with active colloids in vertical cells (*25*, *26*), we confine tens of thousands of fire ants to quasi-2D cells that are 1 m by 10 cm by 1.6 mm and slick the walls with talcum powder to greatly reduce the ants' ability to cling to the cell. This cell is oriented with its long axis vertical, as shown in Fig. 1A, and shaken so that the ants are forced to the bottom of the column, where they form a dense collective with a free surface. From these initial conditions, the collective expands vertically upward over time until it reaches a final height, as shown for a representative experiment in Fig. 1B. We monitor the expansion by measuring the transmission of light through the column over time. We then average the transmission along the horizontal axis and use a calibration curve relating the measured transmission to the ant density, ρ, to obtain spacetime plots with the color indicating the value of ρ, like the one shown in Fig. 1C. Notice that the free surface of the ant column moves vertically upward in a linear fashion before saturating to a fixed average height. At this point, the column has reached a steady state with a clear density gradient due to gravity.

At the top of the column in the steady state, we find an uncompressed ant density of ~9 ants/cm², which corresponds to random close packing of uniform disks with a diameter equal to the average length of an ant, $l = (3.4 \pm 0.7)$ mm. For center-to-center distances less than l, the ants are effectively repulsive, which provides the force needed for the ant column to expand against gravity. This expansion is distinct from that due to the elastic response reported for ant collectives immediately after a short-time compression (*6*, *7*). Ant rearrangements are the root cause of the fluid-like expansion in our ant columns.

In about a third of the column experiments, once the final height is reached, we observe the spontaneous propagation of density waves, such as that highlighted with a dashed box in the spacetime plot in Fig. 1C. Three real-space images of this wave taken 20 s apart are shown in Fig. 2A, and more examples of these waves are shown in movies S1 to S4. Each wave originates near the bottom of the column and propagates toward the free surface. Furthermore, they

Fig. 1. Ant columns. (**A**) Rectangular-prism cell. Dimensions: 1 m by 10 cm by 1.6 mm. Its shortest dimension is only slightly larger than the height of a crawling ant. It is oriented with its longest dimension oriented along the gravitational direction. (**B**) $N \approx 15{,}000$ ants confined in the cell. The walls are slicked with baby powder. The result is a 2D collection of ants at the bottom of the cell with a density that decreases with increasing height. Scale bar, 5 cm. (**C**) Spacetime plot showing the expansion of the ants until they reach a final height. The color represents the density in the ant column. The dashed rectangular box highlights the wave shown in movie S1 and Fig. 2 (A and B).

propagate at a constant speed with a well-defined amplitude, as shown in Fig. 2B, which is a 3D spacetime plot of the density in the column, rotated and inverted to highlight the wave. The waves each persist for several minutes and can propagate for tens of centimeters. Like sound waves and unlike traveling polar bands, no single ant travels for the whole duration of the wave. Instead, ants are swept into the leading edge of the wave, travel with it for a short time, and then drop out from the trailing edge. This is illustrated in Fig. 2C, which shows the vertical component of the velocity of three individual ants as they join and then leave the wave.

To understand the nature of the waves and why they propagate spontaneously, we build a discrete-time simulation. As in Vicsek *et al.*'s original simulation (*10*), ants move at a constant speed and update their orientations based on the average orientation of their nearest neighbors with some noise. To make the simulation more physical, an effective hard body rule is enforced to prevent the ants from overlapping, and a similar interaction is introduced between the ants and the confining walls. Last, we add an effective gravity: Consistent with direct observations from the experiment, if an ant does not find any neighbors below it, it takes a new random orientation downward, ignoring aligning effects. These four rules are enough to produce waves, such as the one shown in Fig. 2D, which move at approximately the same speed as an individual ant and without any appreciable dependence on amplitude.

In our simulations, the traveling waves are instances of local collective motion constrained at the tail end by gravity, which limits the movement of the individual ants. To test whether this is also true in the column experiments, we measure the alignment of the ants as the wave passes. We assign a direction to each ant that points from its abdomen to its head (white arrows in Fig. 2E) and show histograms of the ants' orientation for three different regions on the right side of Fig. 2E: before, during, and after the wave's passage. Notice that in the top bin, through which the wave has not yet passed, the ants have negligible polar alignment, while the ants in the bottom two bins, corresponding to regions where either the wave is located or has just passed, have aligned to move in roughly the same

direction. This indicates that the waves are instances of collective motion, consistent with the simulation results.

There are, however, two important differences between the simulation and experimental results. The first is that the waves are much more common in the simulation; there is rarely a time step in the simulation without at least one wave present in the column. In contrast, ant waves only occurred in about one-third of our 3-hour column experiments, and most of these experiments only exhibited a single wave, implying that their formation is not correctly accounted for in the simulations. We note that, in the simulations, the ants are always moving at a constant speed, but in the experiments, the ants are mostly stationary. These long periods of low activity are punctuated by the sudden bursts of motion that are the waves, reminiscent of the so-called activity cycles observed in rheology experiments with fire ants (*5*), as well as in experiments with other ant species (*27*, *28*).

We thus conjecture that these activity cycles are the root cause of the ant waves. To test this, we confine ants at high density to small circular cells with a radius and height of 2.25 cm and 1.6 mm, respectively. We record the ants with a charge-coupled device camera, threshold the images to identify the ants, and measure the fraction of pixels at a given frame that change value within the next five frames (~1.3 s). We sample this fraction as a function of time to get a rough estimate of how many of the ants are moving throughout a 3-hour experiment. Two examples of these curves for experiments with effective packing fractions of $\phi_{eff} = 3.6$ (blue) and $\phi_{eff} = 2.6$ (red), calculated assuming disks with a diameter equal to l, are shown in Fig. 3A. Notice that both curves have a local maximum at the beginning of the experiment, $t = 0$, reflecting the fact that the ants are all actively moving just after being placed in the cell. As the experiment progresses, many of the pixels stop changing value because some of the ants condense into dense, stationary clusters, reminiscent of the clusters above the wave in Fig. 2A. For example, in Fig. 3 (B and C), there are two images of the ants centered on $t = 117$ min and taken 4.4 min apart in the $\phi_{eff} = 3.6$ experiment. Note that the clusters are almost unchanged between the two images. However, the experiment with a packing fraction of ϕ_{eff}
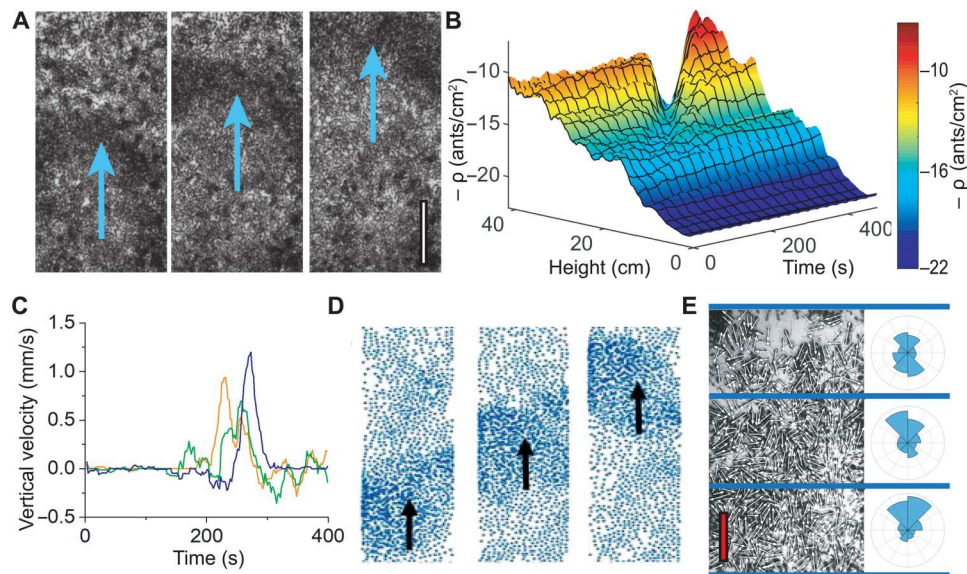
Fig. 2. Ant waves. (**A**) Real-space images of the wave highlighted in Fig. 1C. Each image was taken 20 s apart. Scale bar, 5 cm. (**B**) 3D view of the wave highlighted in Fig. 1C, where the density has been inverted and the surface reoriented to emphasize the constant speed of the wave. Notice that the wave also moves with a constant width and amplitude. (**C**) Vertical velocity of three typical ants before, during, and after the wave passes, showing that the ants activate, travel upward for some time, and then stop moving as they are constrained by gravity. (**D**) Sample wave from our Vicsek model–based simulations. (**E**) The orientations (white arrows) of the ants in three bins while a wave passes through the center bin. Polar histograms for each bin show that the bottom two bins have polar order upward. Scale bar, 1 cm.

= 3.6 has a second peak at $t = 150$ min in Fig. 3A, which indicates that the ants also exhibit a high level of activity at this point in the experiment. At this peak, every ant in the cell is actively moving, just as they were when the experiment began; see Fig. 3 (D and E), taken 8.3 s apart during this peak, and movie S5. A similar peak is absent in the experiment at $\phi_{eff} = 2.6$, reflecting that no activity cycle occurred in this experiment. We have only observed them in experiments with $\phi_{eff} \geq 3.6$; see Fig. 3F. Even when observed, the activity cycles only occur once or twice within the 3-hour duration of our experiments. This helps explain why the waves initially form near the base of the vertical column, where the density is particularly high. It is this sudden change in the ants' motion, which only occurs at very high density, that allows for collective motion. From this perspective, the ant waves are more than density waves. They are also activity waves that form as an activity cycle spreads through the column. These results suggest that shape change and protrusion formation in ant rafts (*24*) could also likely be understood in terms of these intermittent activity cycles; while the ants are mostly stationary, the rafts are nearly circular and only markedly change shape and develop protrusions during an active, collective motion state.

The second important difference between the simulations and the experiments is found by comparing the relationship between the speed, s, and amplitude of the waves. We measure the speed of the experimental ant waves by tracking the peak of the wave in the spacetime plots similar to the one in Fig. 1C. Consistent with the simulation, we find that s is of the same order of magnitude as individual ant speeds, as shown by the scale of the graphs in Figs. 4A and 2C. However, we also find that the experimental waves are nonlinear: larger, denser waves moving more swiftly than the smaller, less dense waves, as also shown in Fig. 4A. This result can be reproduced in the simulation by adding an extra

rule that makes the speed of a particle proportional to the number of interacting neighbors, i.e., to the local density. Figure 4B shows the speeds of the simulated waves as a function of their density when this rule is implemented. This shows that a local density dependence in the speed of individual ants can lead to an amplitude-dependent wave speed.

To gain further insight into the connection between activity, density, and alignment, we quantify the orientations of the ants within a fixed region of the column as a wave passes through it. We plot the average vertical component of the orientation of the ants, $\langle \sin(\theta) \rangle$, as a function of position with respect to the wave frame. In this frame, $y\text{-}y' = 0$ corresponds to the peak of the density wave, and $y\text{-}y' < 0$ corresponds to the ants behind the wave. Notably, there is a clear wave in alignment that lags the density wave, as shown in Fig. 4C. This lag is noteworthy and in contrast to what is found in traveling polar bands of active particles (*16*). The delay between the increase in density and the increase in alignment suggests a frustration between the active aligned ants and the background unaligned inactive ants. Prior work has successfully modeled the effects of ant activity cycles in rheology by considering that the activation rate of the ants is proportional to the number of currently active ants in the region (*5*), which could explain the observed nonlinearity of the waves here. Active ants in the wave are constrained from moving upward by how quickly the ants above them can activate. The activation rate of these frustrating ants then depends on the number of active ants in the area and is the source of the local nonlinearity.

DISCUSSION
The final picture emerging from our experiments and simulations is that the ants propagate waves in activity that result in waves in
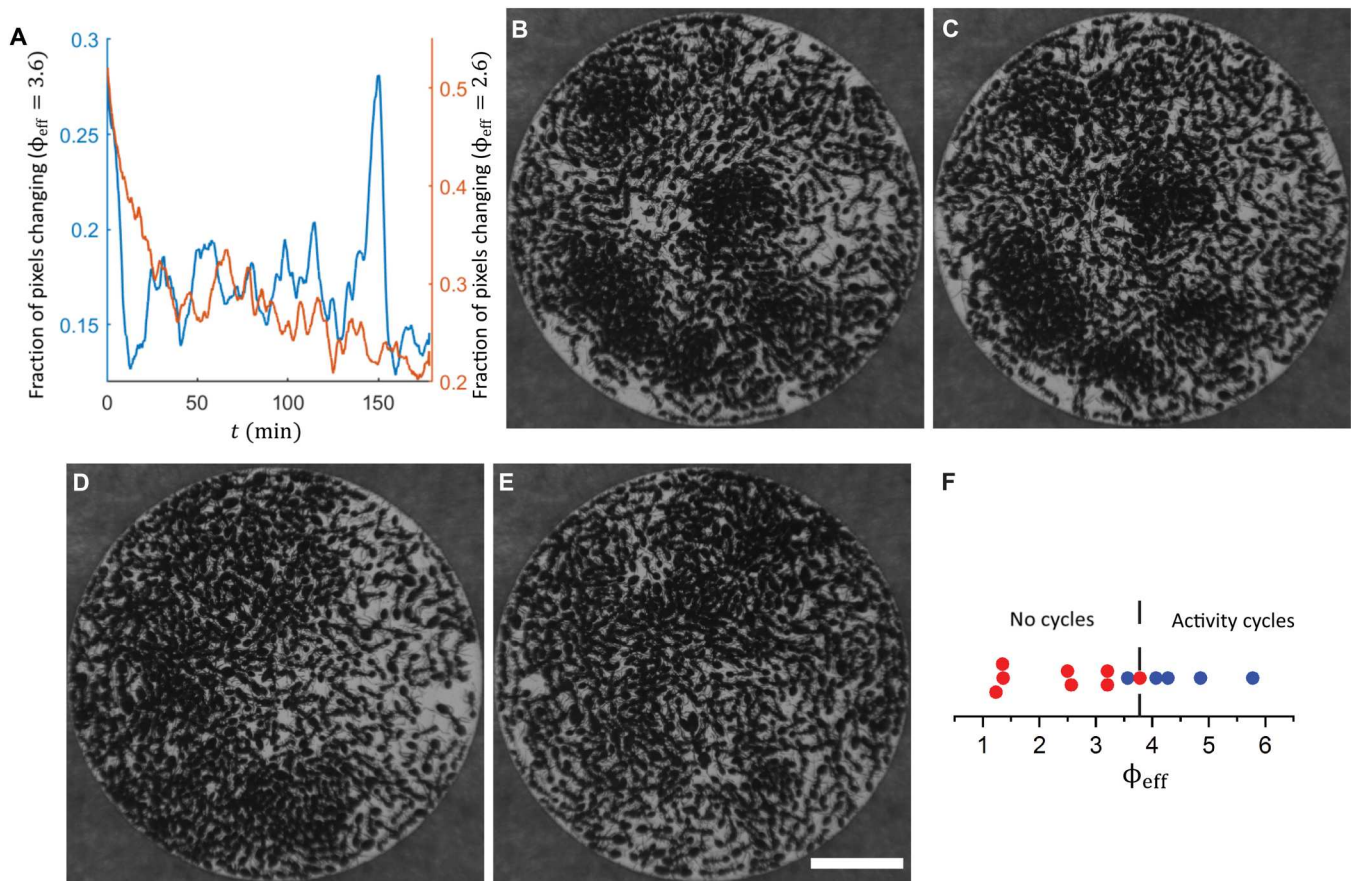
Fig. 3. Activity cycles. (**A**) Fraction of pixels that have changed their threshold result within five frames in trials with $\phi_{eff} = 3.6$ (blue) and $\phi_{eff} = 2.6$ (red). An activity cycle is clearly visible as a strong peak at $t = 150$ min in the trial with $\phi_{eff} = 3.6$. (**B** and **C**) Two images of a small cell taken 4.5 min apart, 117 min into a trial with $\phi_{eff} = 3.6$. The clusters are typical in the ants outside of an activity cycle. (**D** and **E**) Two images taken 8.3 s apart, 150 min into the same trial. Scale bar, 1 cm. (**F**) The presence or lack of activity cycles in trials as a function of effective packing fraction.

alignment and density. The aligned and active ants are part of the wave, constrained from the top by the time it takes the disordered phase to activate and align and at the bottom by a density minimum enforced by gravity. The nonlinearity observed reflects that the ants at the top of the wave align more quickly when they are pressured by larger ant waves from below. The observed waves are similar to sound waves, in that they consist of ants that only briefly travel with the wave. They are also similar to previously studied traveling polar bands, in that they consist of a polarized phase moving through a disordered phase. However, in solutions of the Toner-Tu equations, including those that describe the structure of traveling polar bands, polarization is slaved to density (*17*). In the case of the ants, there are regions near the bottom of the column where the local density is even higher than the density in the waves. However, the inactivity of the ants in those regions allows for the ants to stay locally disordered. The density of the waves is itself not that much higher than the density of the background (see Fig. 4C). Instead, polarization, and therefore collective motion, is a result of locally varying activity, which we conceptualize as the speed an ant would have if it were completely unconstrained. In thinking about the ant waves as activity waves, $\rho_{max} - \rho$ in Fig. 4C can be considered to stand for the density of actively moving ants in the wave, as these are the ants that align and move forward up to the

maximum displacement allowed by gravity. It is then the number of these active ants that controls the activation rate of the ants above them, resulting in the observed nonlinearity.

Spatially varying motility is not uncommon in active systems (*29*, *30*). It is known to lead to motility-induced phase separation, and in colloidal rollers, motility-induced phase separation has been shown to result in solids of stationary particles that propagate as waves through a background of highly motile particles in a direction that is opposite to the motion direction of the background phase (*31*). This is similar to the waves studied here in that the motility of the ants in the wave is different from the background through which the wave propagates. However, unlike the ants, the motility of the colloidal rollers is a function of only density and alignment; it does not depend on an independent "activity" level.

The collective mode reported and discussed here is reflective of an emergent behavior not previously observed before, although emergent behavior is well documented in social insects (*32–36*). We have shown that simple local interaction rules can result in notable group behavior—spontaneously generated nonlinear solitary waves. This hints that these behaviors may be universal over a broad class of active systems, without needing fine-tuning of the local interactions. Furthermore, our results highlight that active matter with intrinsically switchable activity levels could be a
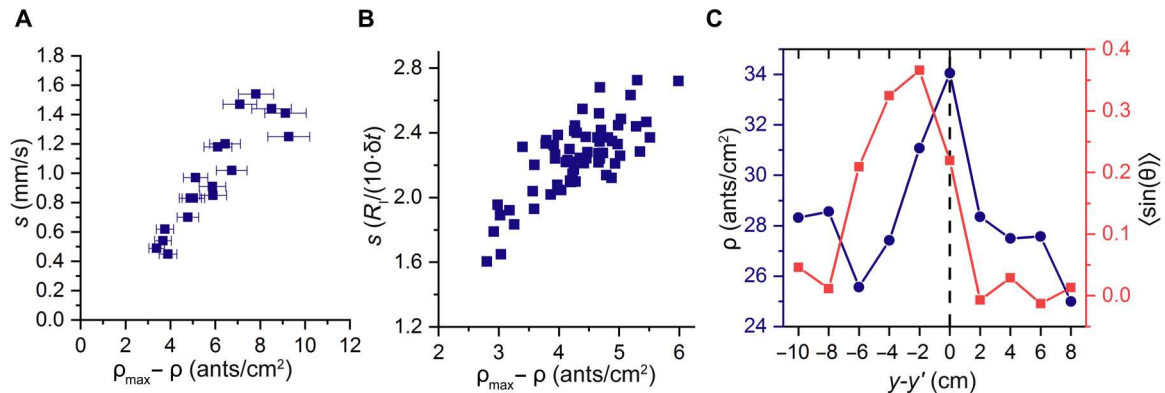
Fig. 4. Nonlinear character of the ant waves. (**A**) Measured speed of the peaks of the density waves as a function of their amplitude. The speed increases with amplitude, and thus, the waves are nonlinear. (**B**) Speed versus amplitude obtained in our Vicsek model–based simulations with an added rule whereby the ants' speed is a function of the local density. The speed of the wave s is normalized by the average speed of all ants in the simulation box, $\langle v_0 \rangle$. (**C**) The average density and the averaged vertical component of the ants' orientation in the wave frame. The angle θ corresponds to an ant's orientation, with $\theta = 0$ being horizontal. The wave is located at $y = y'$. Regions with $y < y'$ are below the wave. Regions with $y > y'$ are regions into which the wave has not yet traveled. A wave in alignment notably lags the density wave.

productive framework to model, for example, stampedes in crowds and herds. Activity cycles in ant rafts, which allow the raft to change shape, reflect switching between inactive and active states. More broadly, our results open the door to addressing how to use varying activity to trigger waves and to perhaps achieve unseen forms of collective behavior and contribute toward understanding the spread and propagation of activity in living structures, tying the study of ants to the existing framework of active matter. Future theoretical work should, at least in part, aim at obtaining a set of relevant partial differential equations that could capture both the generation of the ant waves and their nonlinear behavior.

MATERIALS AND METHODS

Ant collection
Our fire ants were collected from the wild north of Atlanta, GA. We harvest the ants by collecting their mounds and surrounding soil into large buckets and then slowly flooding the buckets over the course of 2 days. This causes the ants to form rafts on the surface of the water. We then transfer rafts from the same wild colony to a wide Tupperware container, where we store the ants between experiments. We cannot store ants that were taken from two different wild colonies together because they kill each other off; this limits the sample sizes that we are able to use in our experiments. While in our care, the ants are given cover in the form of blacked-out halves of petri dishes, a continuous supply of water, and a continuous supply of high-protein chicken or turkey puree.

Ant length and mass
We measured more than 1000 sterile female ants from 10 different colonies and find that the ants have an average length of $l = 3.4$ mm with SD of $\sigma = 0.7$ mm. We also measured the average mass of the ants from five samples of $N \approx 200$ sterile female ants, each taken from different colonies. We found that the average mass of an ant from each of these samples was $m_a = 0.8$ mg and that all five measurements fell between $m = 0.7$ mg and $m = 0.9$ mg. We use this m_a and the mass of a sample of ants that we use in each experiment to estimate the number of ants used in that experiment.

Details of column experiments
We collect most (80 to 90%) of the sterile ants from a Tupperware bin that contains all ants that we collected from a single wild colony. We use as many ants as we can for each experiment because a larger mass of ants allows for waves to propagate longer distances, making the speed and amplitude of the waves easier to accurately measure.

Once we collect the ants from the Tupperware bins, we chill the sample in a refrigerator for a few minutes to make the ants easier to load into the cell. The cell is made of acrylic. Before we load the ants into the cell, we coat the walls of the cell in talcum powder by laying the walls flat and liberally applying the powder, rubbing the powder gently into the walls with gloved hands, and then righting the walls into a vertical position and repeatedly dropping the walls onto the floor from a height of ~10 cm, which knocks off excess powder. The result is a uniform layer of talcum powder on the walls of the cell. We add the ants to the cell by placing the back wall flat and placing ~3-g clumps of ants at different locations and then quickly adding the other walls of the cell and clipping the walls into place.

After each trial, the walls of the cell are wiped down first with water and then with ethanol to ensure that no pheromones are left on the walls. The ants from a given colony are given at least a 40-hour break before they are used in another trial.

Figure 5 summarizes our trials in the column setup, where the x axis shows the date of the trial, and the y axis shows the number of days that we held the ants in captivity before the trial. The size of the points represents the mass of the sample of ants in the trial, and the color of the points represents the presence or lack of waves in the trial. Red points represent trials that produced spontaneous waves within a 2- to 3-hour interval; blue points represent trials in which there were no spontaneous waves, but we tried and succeeded in driving waves by rapidly moving the base of the column upward, compressing the ants at the bottom of the column; and gray points represent trials in which no waves were observed.

Together, we observed waves in of 40 (35%) of our trials. However, many of our trials used ants that were collected during or just after a "severe drought," as defined by the U.S. National Integrated Drought Information System in Kennesaw, GA, which ran from the week of 14 June 2016 to the week of 4 April 2017. These dates are marked in Fig. 5 with vertical black lines. Spontaneous
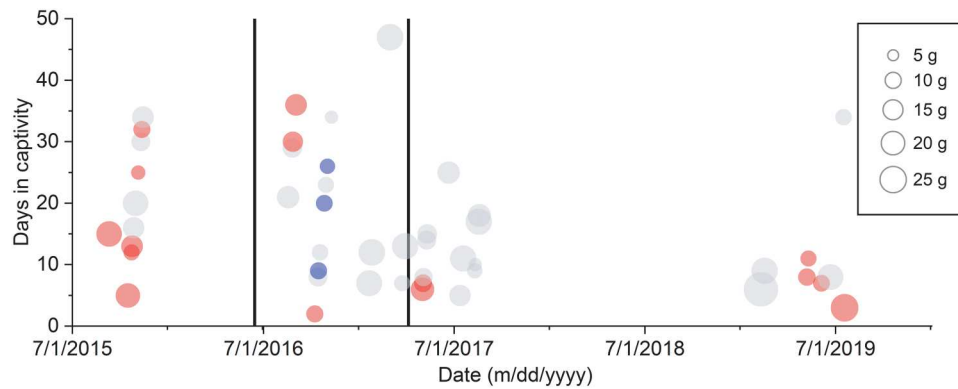
Fig. 5. Graphical illustration of column experiment results. The x axis shows the date of a trial, and the y axis shows how many days the ants had been held in captivity before a trial. The size of the points corresponds to the mass of the sample of ants used in a trial, and the color represents the presence or lack of waves over the course of the trial. Red points represent 2D column trials that produced spontaneous waves within a 2- to 3-hour interval. Blue points represent trials in which there were no spontaneous waves, but we tried and succeeded in driving waves by rapidly moving the base of the column upward, compressing the ants at the bottom of the column. Gray points represent trials in which no waves were observed. The size of the points represents the sample size of ants that were confined to the column. The black lines are the beginning and end of a severe drought in Cobb county, where the ants were collected, as defined by the U.S. National Integrated Drought Information System.

waves formed in only of 17 (12%) of the trials using ants collected more than 6 weeks into the severe drought or in the months immediately after the drought. In contrast, discounting these trials in which the ants must have been affected by the drought, we observed spontaneous waves in of 23 (52%) of our trials. We also noticed that a single colony that produced spontaneous waves in one trial is more likely to produce waves in another trial. Because of these results, we concluded that the health of the colony is the most important factor in the appearance of waves.

Forces on the ants in the column experiments

The forces on an individual ant depend on the situation. A typical, inactive ant can support a substantial portion of its weight via static friction with the walls, as shown in Fig. 6A. The portion of an ants' weight that it can support via static friction depends on the ant's size. Very small ants are unable to brace themselves between the front and back walls, but very large ants can effectively brace themselves against both walls. For example, consider the large ant that supports itself far from the free surface without the aid of any neighbors at the beginning of movie S1. This ant has a length of ~5.7 mm, which is large relative to most of the sterile female fire ants that we use in our experiments; this large size allows it to support itself between the two walls as long as it remains stationary.

When a wave encounters a stationary ant, the moving ants in the wave begin to push on the stationary ant. In response, the static friction forces on the ant change direction to resist the new forces induced by the ant's neighbors within the wave, as shown in Fig. 6B. Therefore, the speed of the wave is determined by how quickly the inactive ants can be activated.
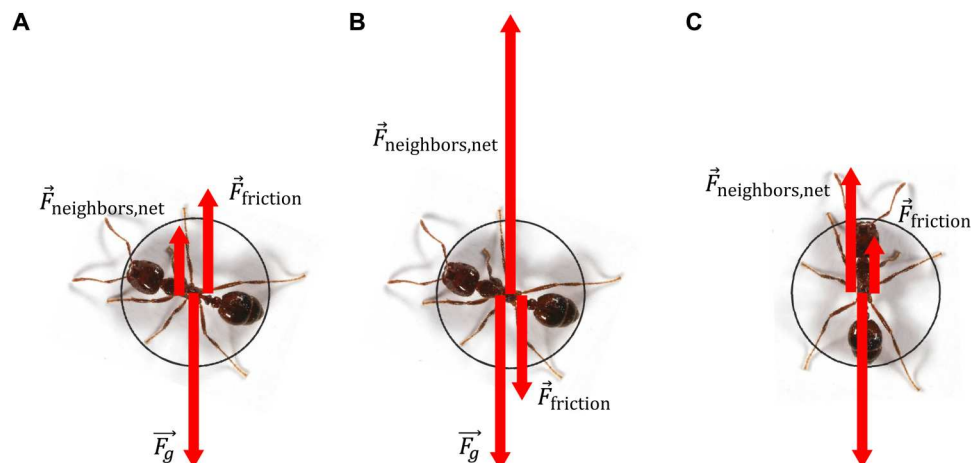
Fig. 6. Proposed forces on the ants. (**A**) For inactive (stationary) ants far from a wave, the ants are supported against gravity by a combination of the net forces from their compressed neighbors and the force of friction with the walls. While the ants are stationary, their grip on the walls is strong enough to help support them against gravity. (**B**) For inactive ants on the leading edge of the waves, the net force of their neighbors is strongly upward as active ants attempt to expand the column. They help resist this force by clinging to the walls. (**C**) For actively moving ants, friction with the walls is negligible, as they slip when they move. Most of their self-propulsion is a result of the ants contracting or expanding their linkages to their nearest neighbors.

Last, active ants seem to be supported almost completely by their neighbors (Fig. 6C) because actively moving ants are not bracing themselves between the two walls and therefore constantly slip. A close examination of the beginning of movie S1 shows that the very large ant above the free surface slips every time it tries to move until it falls to the free surface. In the absence of strong static friction, the active ants must support themselves almost completely via the linkages that they make with their neighbors.

Wave analysis

Images of a backlit column of ants are taken at 1 fps, using the setup shown in Fig. 7A. To begin the analysis, we average the measured intensity horizontally over two columns of interest. The first region is the 10-cm-wide column of ants. This yields an unadjusted average intensity as a function of height and time, $I(y, t)$. The second region is 100 pixels wide and is located to the left of the ant column. This yields a background intensity as a function of height and time, $I_0(y,$
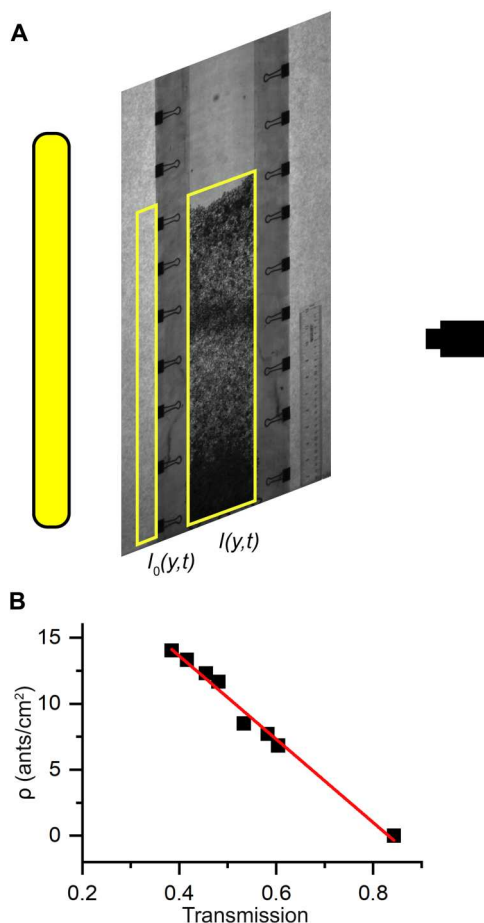
Fig. 7. Experimental methods. (**A**) The cell is filled with ants and oriented with its long axis along the gravitational direction. A large fluorescent light is placed behind the cell with a layer of paper acting as a diffuser. A camera records the intensity of the transmitted light in two columns of interest. The first is $I(y, t)$ containing information about the density of the ant column. The second is $I_0(y, t)$, which we use to normalize our data and compare separate experiments. In a typical experiment, the distance between the camera and the ant column is 3 m. (**B**) The number of counted ants compared to the measured transmission. The red line is a fit used to convert the measured transmission into density.

t). This background intensity allows us to normalize for the fluctuating intensity of our backlight and to compare separate experiments with different levels of lighting. From these two intensities, we calculate the transmission as $T(y, t) = I/I_0$. This quantity is blurred using a 2-cm window in vertical space and 2 s in time to reduce the effects of noise.

Last, we convert the transmission $T(y, t)$ into density using a calibration curve (Fig. 7B). The calibration curve was created by counting ants in regions of interest of 2 cm by 10 cm, spanning the width of the column, and correlating that number to the transmission of the region. The maximum transition that we measure in our cell corresponds to $\rho(y, t) = 0$, but still $T(y, t) \neq 1$, because $I_0(y, t)$ was measured where the light was only transmitted through paper, while $I(y, t)$ was measured where the light had to pass through the paper and two layers of acrylic coated in baby powder. On the other end of our calibration curve, for low T, the ants become so densely packed that we cannot distinguish between ants to count them. Our calibration measurements are well fit by a straight line that we then use to calculate an estimated $\rho(y, t)$ elsewhere in the cell over the course of the whole experiment from the measured $T(y, t)$, similar to the data shown in Fig. 1C. We extrapolate our straight line to account for higher ρ at lower T, although T might no longer be a linear function of ρ at very high densities. High reported densities should then be assumed to be an underestimate of the actual densities, and this underestimation likely increases with increasing ρ. For example, a region with reported density $\rho(y, t) = 25$ ants/cm² is denser than a region with reported density $\rho(y, t) = 20$ ants/cm², but both reported densities are likely underestimates.

To measure the amplitude of a wave, we begin with two images with a 40-s interval between them, such as those shown in Fig. 8 (A and B). This ensures that the wave has traveled more than its own width in between the two frames. We choose images 40 s apart because our slowest measured waves take almost 40 s to travel their own width. The results do not qualitatively change if we select a slightly longer interval. We blur the transmissions of each of these two images using a 2-cm window in the spatial dimensions, convert them to 2D densities using the calibration curve, and take their difference. The resulting difference, similar to the surface shown in Fig. 8C, highlights regions where the density has recently changed. We take the maximum change in density to be the instantaneous amplitude of the wave during the later frame. The location of the maximum change in density in Fig. 8C is marked with an "x." We find that the amplitude remains relatively constant over the last 50 s before the wave hits the free surface, but typically increases slightly over time, similar to the example shown in Fig. 8D. We lastly take the average of the instantaneous amplitudes over the last 50 s as the amplitude of the wave, $\rho_{max} - \rho$ in Fig. 4A. We take measured values with an error of 10% to account for the drift of the instantaneous amplitude.

To measure the speed of the wave, we find the time for which the maximum occurs for every height in $\rho(y, t)$, $t_m(y)$, like the black curve in Fig. 8E. From $t_m(y)$, we pick the lowest height above which the wave travels at a clearly constant velocity, h_b, and then fit $t_m(y)$ from $y = h_b$ to the free surface with a line, like the red line in Fig. 8E. We take the slope of this line to be the speed of the wave, s. The errors calculated from these linear fittings would lie within the points in Fig. 4A.
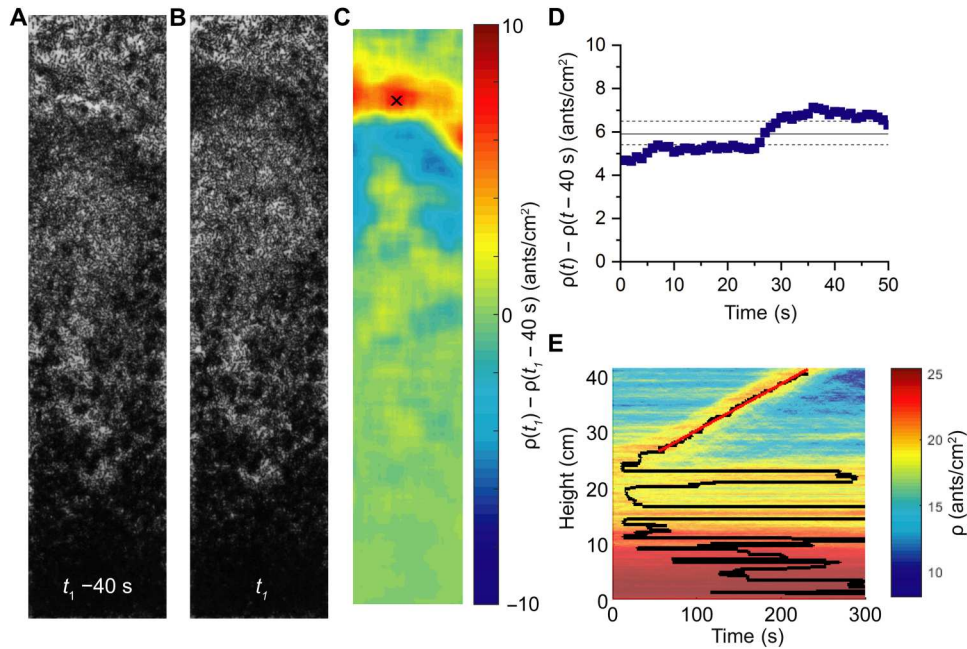
Fig. 8. Amplitude and speed measurements. (**A**) An image of a wave as it travels toward the free surface. (**B**) An image of the same wave after an interval of 40 s. (**C**) The difference in the measured density from the two frames of the experiment. The location of the maximum change in density is marked with an x. (**D**) Measured instantaneous amplitude over the 50 s before the wave reaches the free surface. (**E**) Spacetime diagram of the wave as it travels toward the free surface. The black curve shows the time with the maximum measured density as a function of height. The red line is a linear fit of the black curve for the vertical positions in which the wave is moving at a constant velocity.

Ant speed analysis

The single-ant speeds shown in Fig. 2C, are measured by tracking the position of the ants over time at a rate of 0.5 fps, as seen in movie S6. The speeds of the ants are then reported as the vertical component of their velocity time averaged over 16 s.

Simulation

We constructed simulations of the ants in discrete time with continuous spatial coordinates, following the precedent of the Vicsek model. After each time step, Δt, all ants update their orientations and velocities simultaneously based on their neighbors' positions and velocities from the previous step, with the following rules being executed in order. As a result, rules later in the list can override behaviors earlier in the list.

1) Basic alignment. The ant updates its orientation based on the orientation of the ants within its interaction radius, R_I. We then have

$$\theta(t + \Delta t) = \langle \theta(t) \rangle_{R_I} + \Delta\theta$$

$$v_x(t + \Delta t) = v_0 \cos[\theta(t + \Delta t)]$$

$$v_y(t + \Delta t) = v_0 \sin[\theta(t + \Delta t)]$$

where $\theta(t)$ is the orientation of the ant in the previous time step, with $\theta(t) = 0$ corresponding to horizontal, v_0 is its speed, and $v_x(t + \Delta t)$ and $v_y(t + \Delta t)$ are the updated velocities in the horizontal and vertical directions, respectively. The time step Δt is defined in terms of the ratio R_I/v_0; in our simulations, we take $\Delta t = 0.1 R_I/v_0$, as

chosen by Vicsek *et al.* (*10*) in their seminal work. We find that if we continue to decrease the time steps, the simulations no longer produce waves. Instead, the entire column of ants aligns very quickly so that there is never a localized group of ants that are more strongly aligned than the rest of the column. We calculate $\langle \theta(t) \rangle_{R_I}$ as the two-argument inverse tangent of the average vertical and horizontal components of the velocities of the neighboring ants inside the ant of interest's interaction radius, R_I

$$\langle \theta(t) \rangle_{R_I} = \arctan2(\langle v_y \rangle_{R_I}, \langle v_x \rangle_{R_I})$$

The quantity $\Delta\theta$ is a uniformly distributed noise term that ranges from $-\eta \leq \Delta\theta \leq \eta$ so that the particles undergo Brownian motion when $\eta = \pi$. For the data and movies here, $\eta = 0.8$ rad.

2) Gravity restriction. If there is no ant within the sector of the circle bounded by R_I with $-\frac{3\pi}{4} \leq \theta \leq -\frac{\pi}{4}$, the ant drifts downward

$$v_x(t + \Delta t) = v_0 \cos(\Delta\theta_G)$$

$$v_y(t + \Delta t) = v_0 \sin(\Delta\theta_G)$$

where $\Delta\theta_G$ is a uniformly distributed random angle within $\left[-\frac{\pi}{4}, -\frac{3\pi}{4}\right]$.

3) Short-range repulsion. If another ant is found within a smaller body radius $R_B < R_I/2$, a coordinate transformation is performed so that the ant loses the component of its velocity that would bring it radially closer to the neighboring repelling ant and adopts a small velocity radially away from the neighbor so that it will leave the body radius in the following time step. The tangential velocity of the ant

relative to its neighbor stays unchanged. We take

$$\vec{v}_r = (R_B - r)/(2\Delta t)\,\hat{r}$$
$$v_\theta \text{ unchanged}$$

where r is the distance between the two ants and $\hat{r}$ is the unit vector along the radial direction. The choice of the factor of 1/2 ensures that the two ants will have a pair distance $r \geq R_B$ during the next time step when $\Delta t = 0.1R_I/v_0$. We then use the inverse coordinate transform to update $v_x(t + \Delta t)$ and $v_y(t + \Delta t)$.

4) Wall interaction. If the ant approaches a wall and gets within a distance of $R_I/2$ from the wall, it immediately loses the component of its velocity that would move it toward the wall. In this case

$$v_x = 0 \text{ or } v_y = 0$$

After all the ants have updated their velocities, their positions are updated to be

$$x(t + \Delta t) = x(t) + v_x(t + \Delta t)\,\Delta t$$

$$y(t + \Delta t) = y(t) + v_y(t + \Delta t)\,\Delta t$$

The alignment rule naturally leads to flocking of the simulated ants, and the short-range repulsion rule prevents these flocks from collapsing to a single point in the corners of the cell, as seen in movie S7. The gravity rule allows for the switching in behavior that we need to observe the waves. In the simulation, the waves are instances of collective motion switched on and off by the constraints of density.

The four rules above are enough to generate waves, but the resulting waves are not nonlinear. To better capture the results of our experimental measurements, we can modify the velocity of the ants

$$v_x(t + \Delta t) = v_0\cos[\theta(t + \Delta t)]$$

$$v_y(t + \Delta t) = v_0\sin[\theta(t + \Delta t)]$$

$$v_0 = C_v\,(1 + n)$$

where n is the number of ants found within the ants' interaction radius R_I and C_v is a constant chosen to ensure that the ants still move with an average speed $\langle v_0 \rangle$ that satisfies $10\langle v_0 \rangle \Delta t = R_I$. This modification allows for stronger and nonlinear waves, such as those seen in movie S8. We note that the selection of C_v affects the slope of the nonlinearity. We choose to select C_v such that the average velocity of the particles matched the conditions in our simulations without the density-dependent speed. We thus choose C_v so that $\langle v_0 \rangle = 0.1R_I/\Delta t$, which corresponds to the speed of the ants in the simulations in which we do not include the density dependence of v_0. We do this so that the results of the nonlinear and linear simulations can be easily compared.

Alignment measurements

To measure alignment, we begin with a region of interest, sufficiently far from both the walls and the free surface, through which a wave passes. The region of interest measures 3.2 cm by 5.5 cm, horizontally and vertically, and contains about 500 ants. For each of the eight frames, spaced about 20 s apart, the alignment and position of each ant in the region of interest are determined by associating an arrow to each ant, as seen in Fig. 9A. The arrow points from the posterior tip of the ant's abdomen to the center of their mandibles. We use the center of the line of the arrow as the position of the ant and treat the direction of the arrow as the orientation of the ant. To obtain better statistics, we shift a series of images into the wave frame. This is done by considering the average speed of the wave, calculating where the center of the wave lies for each frame, and translating the vertical coordinate of the frame so that the center of the wave would lie at $y = 0$. Once the frames are shifted, the ants are binned by vertical position into 11 bins of 2 cm, containing 360 ants on average. For each of these bins, we calculate the
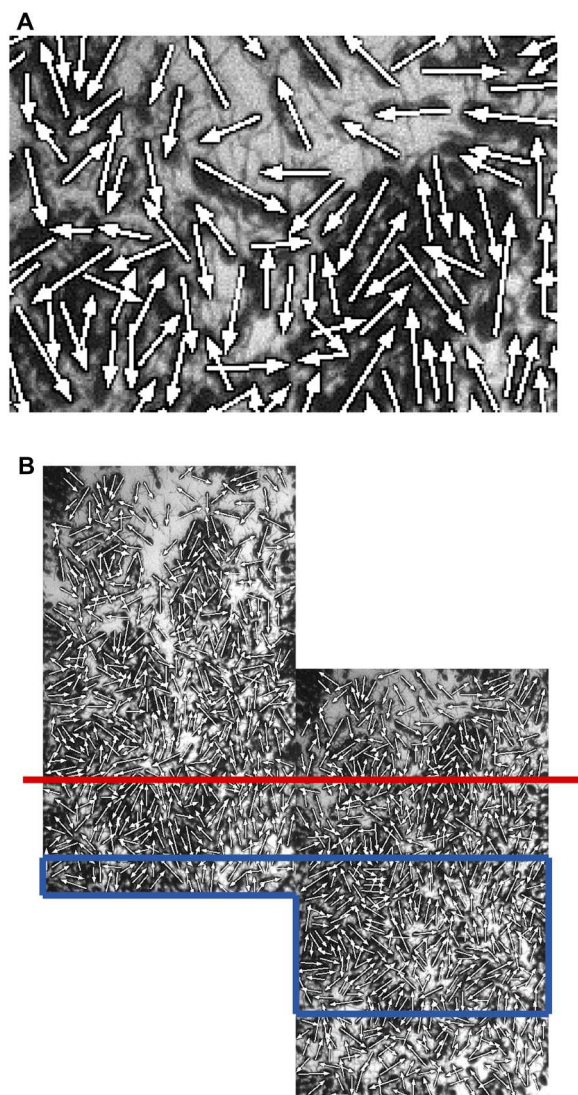
Fig. 9. Alignment analysis. (**A**) Ants in the column with arrows associated to each of them. The arrows are used to measure the position and orientation of the ants. (**B**) For better statistics when calculating alignment, images are shifted into the wave frame. In this frame, the peak of the wave lies at $y = y'$ on the red line shown. The blue outline represents one of the bins ($-3\ \text{cm} < y - y' < -1\ \text{cm}$) in two of the images used for calculating the alignment and density of the ants in Fig. 4C.

alignment of the ants as $\langle \sin\theta \rangle$ and the density as N/A_{tot}, where A_{tot} is the total area available to the ants in that bin, and θ is the orientation of an ant measured from the horizontal. An example of this translation to the wave frame and the borders of a bin in two images are shown in Fig. 9B.

Activity cycle analysis

To detect the activity cycles, we start by subtracting the background from the images, which we define on a pixel-by-pixel basis as the maximum detected intensity over the course of the experiment. After subtracting the background, we threshold each of the images to identify the pixels that correspond to the ants: $I_{\text{thresh}}(x, y, t) = 1$ if the pixel is part of an ant and $I_{\text{thresh}}(x, y, t) = 0$ if the pixel is not part of an ant. We then calculate the number of moving pixels

$$M(t) = \frac{\sum_{x,y} \mid I_{\text{thresh}}(x, y, t) - I(x, y, t + \Delta t) \mid}{2 \sum_{x,y} I(x, y, t)}$$

where the factor of 2 accounts for the fact that we count both pixels that an ant moves into and pixels that an ant moves out of. We choose $\Delta t = 5$ frames ≈ 1.3 s. Changing Δt by small amounts does not qualitatively affect our results. We report $M(t)$ as the fraction of pixels changing in Fig. 3A.

Supplementary Materials

This PDF file includes:
Legends for movies S1 to S8

Other Supplementary Material for this manuscript includes the following:
Movies S1 to S8

REFERENCES AND NOTES

1. M. Nagy, Z. Akos, D. Biro, T. Vicsek, Hierarchical group dynamics in pigeon flocks. *Nature* **464**, 890–893 (2010).

2. T. Mora, A. M. Walczak, L. Del Castello, F. Ginelli, S. Melillo, L. Parisi, M. Viale, A. Cavagna, I. Giardina, Local equilibrium in bird flocks. *Nat. Phys.* **12**, 1153–1157 (2016).

3. Y. Wu, A. D. Kaiser, Y. Jiang, M. S. Alber, Periodic reversal of direction allows Myxobacteria to swarm. *Proc. Natl. Acad. Sci. U.S.A.* **106**, 1222–1227 (2009).

4. A. Sokolov, M. M. Apodaca, B. A. Grzybowski, I. S. Aranson, Swimming bacteria power microscopic gears. *Proc. Natl. Acad. Sci. U.S.A.* **107**, 969–974 (2010).

5. M. Tennenbaum, A. Fernandez-Nieves, Activity-driven changes in the mechanical properties of fire ant aggregations. *Phys. Rev. E* **96**, 052601 (2017).

6. F. J. Vernerey, T. Shen, S. L. Sridhar, R. J. Wagner, How do fire ants control the rheology of their aggregations? A statistical mechanics approach. *J. R. Soc. Interface* **15**, 20180642 (2018).

7. M. Tennenbaum, Z. Liu, D. Hu, A. Fernandez-Nieves, Mechanics of fire ant aggregations. *Nat. Mater.* **15**, 54–59 (2016).

8. M. C. Marchetti, J. F. Joanny, S. Ramaswamy, T. B. Liverpool, J. Prost, M. Rao, R. A. Simha, Hydrodynamics of soft active matter. *Rev. Mod. Phys.* **85**, 1143–1189 (2013).

9. J. Toner, Y. Tu, Long-range order in a two-dimensional dynamical XY model: How birds fly together. *Phys. Rev. Lett.* **75**, 4326–4329 (1995).

10. T. Vicsek, A. Czirók, E. Ben-Jacob, I. Cohen, O. Shochet, Novel type of phase transition in a system of self-driven particles. *Phys. Rev. Lett.* **75**, 1226–1229 (1995).

11. G. Grégoire, H. Chaté, Onset of collective and cohesive motion. *Phys. Rev. Lett.* **92**, 025702 (2004).

12. A. J. W. Ward, D. J. T. Sumpter, I. D. Couzin, P. J. B. Hart, J. Krause, Quorum decision-making facilitates information transfer in fish shoals. *Proc. Natl. Acad. Sci. U.S.A.* **105**, 6948–6953 (2008).

13. Y. Tu, J. Toner, M. Ulm, Sound waves and the absence of galilean invariance in flocks. *Phys. Rev. Lett.* **80**, 4819–4822 (1998).

14. J. Toner, Y. Tu, S. Ramaswamy, Hydrodynamics and phases of flocks. *Ann. Phys.* **318**, 170–244 (2005).

15. D. Geyer, A. Morin, D. Bartolo, Sounds and hydrodynamics of polar active fluids. *Nat. Mater.* **17**, 789–793 (2018).

16. H. Chaté, F. Ginelli, G. Grégoire, F. Raynaud, Collective motion of self-propelled particles interacting without cohesion. *Phys. Rev. E* **77**, 046113 (2008).

17. J. B. Caussin, A. Solon, A. Peshkov, H. Chaté, T. Dauxois, J. Tailleur, V. Vitelli, D. Bartolo, Emergent spatial structures in flocking models: A dynamical system insight. *Phys. Rev. Lett.* **112**, 148102 (2014).

18. A. Bricard, J. B. Caussin, N. Desreumaux, O. Dauchot, D. Bartolo, Emergence of macroscopic directed motion in populations of motile colloids. *Nature* **503**, 95–98 (2013).

19. A. Martín-Gómez, D. Levis, A. Díaz-Guilera, I. Pagonabarraga, Collective motion of active Brownian particles with polar alignment. *Soft Matter* **14**, 2610–2618 (2018).

20. A. P. Solon, H. Chaté, J. Tailleur, From phase to microphase separation in flocking models: The essential role of nonequilibrium fluctuations. *Phys. Rev. Lett.* **114**, 068101 (2015).

21. H. Chaté, Dry aligning dilute active matter. *Annu. Rev. Condens. Matter Phys.* **11**, 189–212 (2020).

22. N. J. Mlot, C. A. Tovey, D. L. Hu, Fire ants self-assemble into waterproof rafts to survive floods. *Proc. Natl. Acad. Sci. U.S.A.* **108**, 7669–7673 (2011).

23. P. C. Foster, N. J. Mlot, A. Lin, D. L. Hu, Fire ants actively control spacing and orientation within self-assemblages. *J. Exp. Biol.* **217**, 2089–2100 (2014).

24. R. J. Wagner, K. Such, E. Hobbs, F. J. Vernerey, Treadmilling and dynamic protrusions in fire ant rafts. *J. R. Soc. Interface* **18**, 20210213 (2021).

25. J. Palacci, C. Cottin-Bizonne, C. Ybert, L. Bocquet, Sedimentation and effective temperature of active colloidal suspensions. *Phys. Rev. Lett.* **105**, 088304 (2010).

26. F. Ginot, I. Theurkauff, D. Levis, C. Ybert, L. Bocquet, L. Berthierand, C. Cottin-Bizonne, Nonequilibrium equation of state in suspensions of active colloids. *Phys. Rev. X* **5**, 011004 (2015).

27. B. J. Cole, Short-term activity cycles in ants: Generation of periodicity by worker interaction. *Am. Nat.* **137**, 244–259 (1991).

28. S. Boi, I. D. Couzin, N. D. Buono, N. R. Franks, N. F. Britton, Coupled oscillators and activity waves in ant colonies. *Proc. R. Soc. Lond. B.* **266**, 371–378 (1999).

29. F. D. C. Farrell, M. C. Marchetti, D. Marenduzzo, J. Tailleur, Pattern formation in self-propelled particles with density-dependent motility. *Phys. Rev. Lett.* **108**, 248101 (2019).

30. M. Van Der Linden, L. Alexander, D. Aarts, O. Dauchot, Interrupted motility induced phase separation in aligning active colloids. *Phys. Rev. Lett.* **123**, 098001 (2019).

31. D. Geyer, D. Martin, J. Tailleur, D. Bartolo, Freezing a flock: Motility-induced phase separation in polar active liquids. *Phys. Rev. X* **9**, 031043 (2019).

32. A. Gelblum, I. Pinkoviezky, E. Fonio, N. S. Gov, O. Feinerman, Emergent oscillations assist obstacle negotiation during ant cooperative transport. *Proc. Natl. Acad. Sci. U.S.A.* **113**, 14615–14620 (2016).

33. G. Kastberger, E. Schmelzer, I. Kranner, Social waves in giant honeybees repel hornets. *PLOS ONE* **3**, e3141 (2008).

34. L. Li, H. Peng, J. Kurths, Y. Yang, H. J. Schellnhuber, Chaos–order transition in foraging behavior of ants. *Proc. Natl. Acad. Sci.* **111**, 8392–8397 (2014).

35. S. C. Nicolis, J. Fernández, C. Pérez-Penichet, C. Noda, F. Tejera, O. Ramos, D. J. T. Sumpter, E. Altshuler, Foraging at the edge of chaos: Internal clock versus external forcing. *Phys. Rev. Lett.* **110**, 268104 (2013).

36. F. Tejera, A. Reyes, E. Altshuler, Uninformed sacrifice: Evidence against long-range alarm transmission in foraging ants exposed to localized abduction. *Eur. Phys. J. Spec. Top.* **225**, 663–668 (2016).